ADVANCED MATERIALS INTERFACES
Open Access
www.advmatinterfaces.de

Investigating Impacts of Local Pressure and Temperature on CVD Growth of Hexagonal Boron Nitride on Ge(001)/Si

Max Franck, Jarek Dabrowski, Markus Andreas Schubert, Dominique Vignaud, Mohamed Achehboune, Jean-François Colomer, Luc Henrard, Christian Wenger, and Mindaugas Lukosius**

The chemical vapor deposition (CVD) growth of hexagonal boron nitride (hBN) on Ge substrates is a promising pathway to high-quality hBN thin films without metal contaminations for microelectronic applications, but the effect of CVD process parameters on the hBN properties is not well understood yet. The influence of local changes in pressure and temperature due to different reactor configurations on the structure and quality of hBN films grown on Ge(001)/Si is studied. Injection of the borazine precursor close to the sample surface results in an inhomogeneous film thickness, attributed to an inhomogeneous pressure distribution at the surface, as shown by computational fluid dynamics simulations. The additional formation of nanocrystalline islands is attributed to unfavorable gas phase reactions due to the radiative heating of the injector. Both issues are mitigated by increasing the injector-sample distance, leading to an 86% reduction in pressure variability on the sample surface and a 200 °C reduction in precursor temperature. The resulting hBN films exhibit no nanocrystalline islands, improved thickness homogeneity, and high crystalline quality (Raman FWHM = 23 cm^{-1}). This is competitive with hBN films grown on other non-metal substrates but achieved at lower temperature and with a low thickness of only a few nanometers.

1. Introduction

The 2D insulator hexagonal boron nitride (hBN) has a range of promising applications, including deep ultraviolet optoelectronics,[1,2] tunnel barriers in tunnel devices,[3,4] and protection layers for high-mobility graphene.[5–8] The most common method for synthesizing large-area, high-quality hBN, besides mechanical exfoliation, is chemical vapor deposition (CVD) on catalytic transition metal substrates like Cu and Ni.[9–13] However, transfer of the hBN layers is required for device fabrication, which was shown to leave residual metal contaminations at concentrations unacceptable for Si technology integration.[14–16] Consequently, the growth of hBN thin films directly on CMOS-compatible substrates, such as silicon-based substrates, germanium, or dielectrics, is desirable. That way, transferred hBN films are completely free of metal contaminations, and depending on the application, the need for transfer could be eliminated altogether, making fabrication processes much more scalable and cost-effective.

On sapphire and silicon substrates, successful growth ranging from randomly oriented, nanocrystalline hBN films several hundred nanometers or even micrometers thick[17–19] to well-aligned, layered growth with thicknesses from a few to several dozen layers[20–25] has been reported. For applications like graphene encapsulation in hBN/graphene/hBN heterostructures, well-aligned few-layer hBN films are preferred,[3,26] but the precise control of the number of layers remains challenging on these substrates. Lately, Ge has also been explored as a new non-metal growth substrate with catalytic activity[27] for high-quality

M. Franck, J. Dabrowski, M. A. Schubert, C. Wenger, M. Lukosius
IHP – Leibniz-Institut für innovative Mikroelektronik
Im Technologiepark 25, 15236 Frankfurt (Oder), Germany
E-mail: franck@ihp-microelectronics.com;
lukosius@ihp-microelectronics.com

The ORCID identification number(s) for the author(s) of this article can be found under https://doi.org/10.1002/admi.202400467

DOI: 10.1002/admi.202400467

D. Vignaud
University of Lille
CNRS
University Polytechnique Hauts de France
UMR 8520-IEMN
Lille F-59000, France

M. Achehboune, J.-F. Colomer, L. Henrard
Laboratoire de Physique du Solide
Namur Institute of Structured Matter
University of Namur
Rue de Bruxelles 61, Namur 5000, Belgium

C. Wenger
Semiconductor Materials
BTU Cottbus-Senftenberg
Platz der Deutschen Einheit 1, 03046 Cottbus, Germany

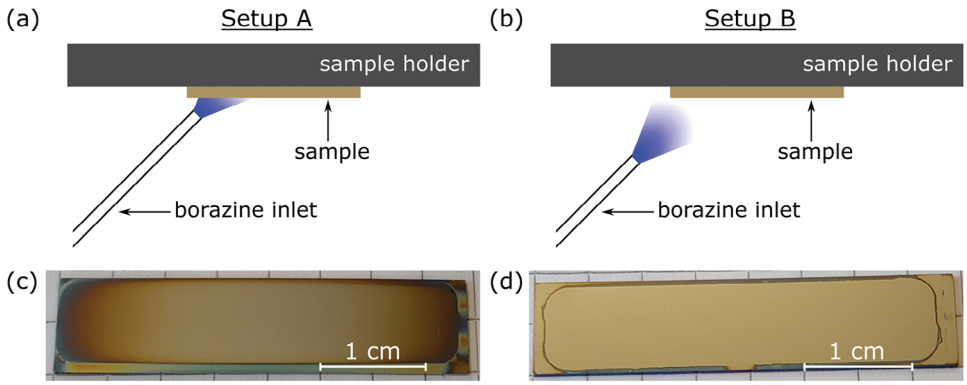

Figure 1. a,b) Schematics of the two reactor configurations investigated. c,d) Optical photographs of samples grown with Setup A and B, respectively.

graphene.[28–30] On the other hand, reports for hBN synthesis on Ge substrates are scarce, and a catalytic effect of Ge has not been definitively proven. Nevertheless, low-pressure CVD growth of polycrystalline monolayer hBN using ammonia borane as the precursor has been reported previously.[31–33] The formation of triangular islands with 90° and 180° rotational symmetry on Ge(001) and Ge(110), respectively, was observed,[31,32] and monolayer hBN was found to provide significant passivation against oxidation of the Ge surface.[33] However, the effect of CVD process parameters like temperature, pressure, or flow rate on the hBN properties was not investigated.

Recognizing this deficit, the influence of reactor pressure and growth temperature on the CVD synthesis of hBN films on Ge(001) substrates was studied recently, using borazine as the precursor.[34] A clear improvement in crystalline quality with increasing growth temperature was observed. While well-oriented, layered growth of multilayer hBN was achieved at high temperature and 0.1 Pa, the formation of a large number of islands with randomly oriented nano-crystallites was also observed. The conditions leading to the different growth modes (well-aligned layers vs randomly oriented nano-crystallites) of hBN on Ge substrates have not been understood yet. In addition to the reactor pressure and growth temperature, gas phase reactions can be critical to CVD growth,[35] and the exact chemical species that participate in the growth of hBN from borazine are still unknown. Consequently, there is a need for further development of hBN thin film growth processes on Ge substrates. In particular, understanding how growth mechanisms respond to changes in temperature and pressure is crucial for tailoring the properties of hBN.

In this work, we study the influence of local changes in pressure and temperature due to different reactor configurations on the structure and quality of hBN films grown on Ge(001)/Si substrates. The borazine precursor is delivered to the reactor via an injector tube, the position of which can affect the local precursor partial pressure at the sample surface, as well as the gas temperature, thus influencing gas phase reactions. It was found that the morphology, structure, and crystalline quality of hBN films grown with two different reactor configurations differ significantly in response to these effects. Computational fluid dynamics (CFD) simulations of the experimental setups helped to identify the dominant effects from a fluid dynamics and heat transport perspective.

2. Results and Discussion

The two reactor configurations studied in this work, named Setup A and Setup B, are shown schematically in **Figure 1**a,b. In Setup A, the borazine injector is positioned very close to the sample surface (distance ≈3 cm) and pointing toward one end of the sample (this is due to the positioning of the flanges on the reactor chamber). For Setup B, the injector is moved 5 cm away from the sample surface along its axis. The same growth parameters were used for both setups, as detailed in the Experimental section.

The hBN films grown with reactor setup A exhibit inhomogeneous film thickness, visible as a color gradient, as seen in the photograph in Figure 1c. The gradient suggests increasing film thickness at the outer ends of the sample, which are closest to the borazine inlet. Due to rotation around the center of the sample during growth, the thickness gradient is mirrored on the other side of the sample. On the other hand, Setup B yields a thinner and more homogeneous hBN film, which is evident to the eye as no discoloration of the Ge substrate, as shown in Figure 1d. The sample exhibits no interference colors, pointing to a relatively thin film of at most 45 nm, assuming a refractive index of ≈2.2,[36] even at the edges of the sample. This indicates a noticeably lower overall growth rate with setup B. The additional discolorations at the outer edges of the samples (yellow-blue areas in Figure 1c and dark lines in Figure 1d) mark the contact area with the sample holder, which is not considered in the analysis.

The film thickness, structure, and crystalline quality are investigated in detail via high-resolution cross section transmission electron microscopy (TEM). **Figure 2**a shows a low-magnification overview image of the center region of a sample grown with Setup A. The hBN film mainly consists of relatively large islands, up to 100 nm in diameter and 20 nm in height, and some flat, layered regions between the islands. The islands are nanocrystalline (Figure 2b), with randomly oriented crystallites ≈2–5 nm in size, as described recently.[34] For Setup B, the formation of the nanocrystalline islands is suppressed, as shown in Figure 2d. The high-resolution image in Figure 2e reveals well-oriented, layered growth of hBN and a film thickness of 4.2 nm after a growth time of 240 min. The film thickness is not entirely homogeneous, as evident from the overview image (Figure 2d), and varies between 1.7 nm (5 layers) and 4.6 nm (14 layers). Nevertheless, this is a significant improvement compared to the nanocrystalline islands

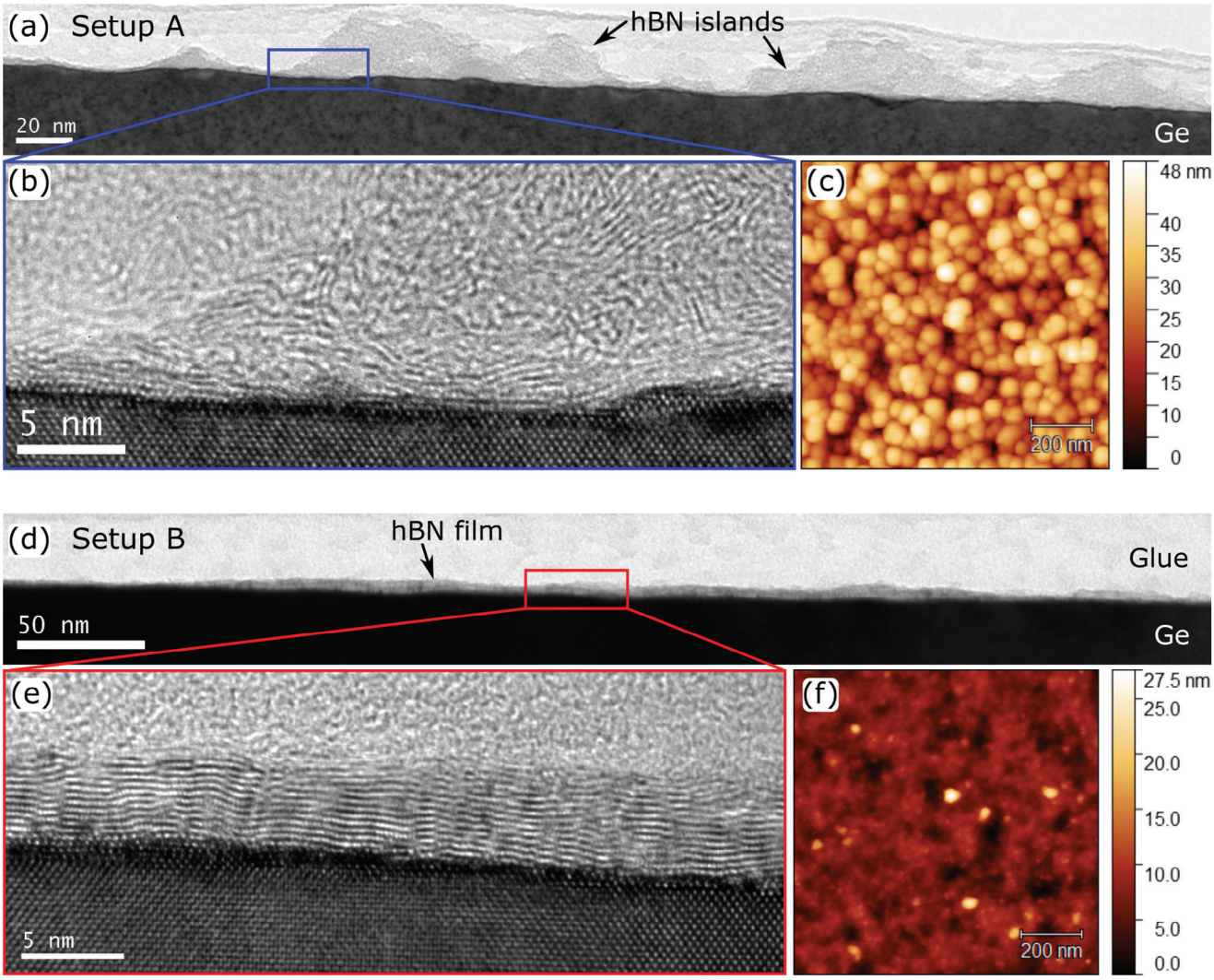

Figure 2. Cross section TEM images of hBN films grown with a,b) Setup A and d,e) Setup B, as well as c,f) corresponding AFM images.

from Setup A, and the film thickness is in the range suitable for the envisioned application of graphene encapsulation layers.

The morphology of the sample shown in Figure 2a (grown with Setup A) is dominated by the large nanocrystalline islands, as seen in the corresponding atomic force microscopy (AFM) image in Figure 2c. The RMS roughness is 7.4 nm. For Setup B, AFM images (Figure 2f) show the absence of large islands, and consequently, the RMS roughness is strongly reduced to 2.1 nm. Nevertheless, a few smaller islands are visible, with approximate heights of 10–15 nm and lateral sizes of 30–60 nm. If the islands are omitted from the calculation, an RMS roughness of 1.8 nm is obtained, demonstrating that the surface morphology is now dominated by the roughness of the layered hBN film rather than by the islands. This, in turn, is at least partially caused by the roughening of the Ge substrate during the growth process, which can also be observed in the TEM images, due to the growth temperature being very close to the melting point of germanium. Before the hBN growth process, the RMS roughness of the epitaxial Ge film is <0.5 nm.[37] However, to obtain the highest quality hBN films, the growth temperature needs to be as high as possible, and reducing the temperature to control the Ge roughening would result in a partially amorphous hBN film.[34]

The smaller islands found in the AFM images for Setup B were investigated in more detail by TEM and energy-dispersive X-ray spectroscopy (EDX). **Figure 3**a shows a high-resolution cross section TEM image of one of these islands, revealing an amorphous structure covered by layered hBN. Additionally, EDX maps (Figure 3b–d) show an inhomogeneous distribution of N and B atoms in the islands. There is a notable nitrogen deficiency in the amorphous parts of the island, while the layered parts are more stoichiometric, as shown by X-ray photoelectron spectroscopy (XPS) toward the end of this section. The difference in crystallinity suggests that the formation mechanism of these islands differs from that of the nanocrystalline islands found in the samples grown with Setup A (Figure 2a,b) and confirms that the latter are indeed suppressed completely with Setup B. Moreover, the fact that layered hBN covers the islands for Setup B could indicate that the amorphous part forms in the early stages of film growth and is later overgrown by the forming hBN film. This was corroborated by conducting a growth experiment with a growth

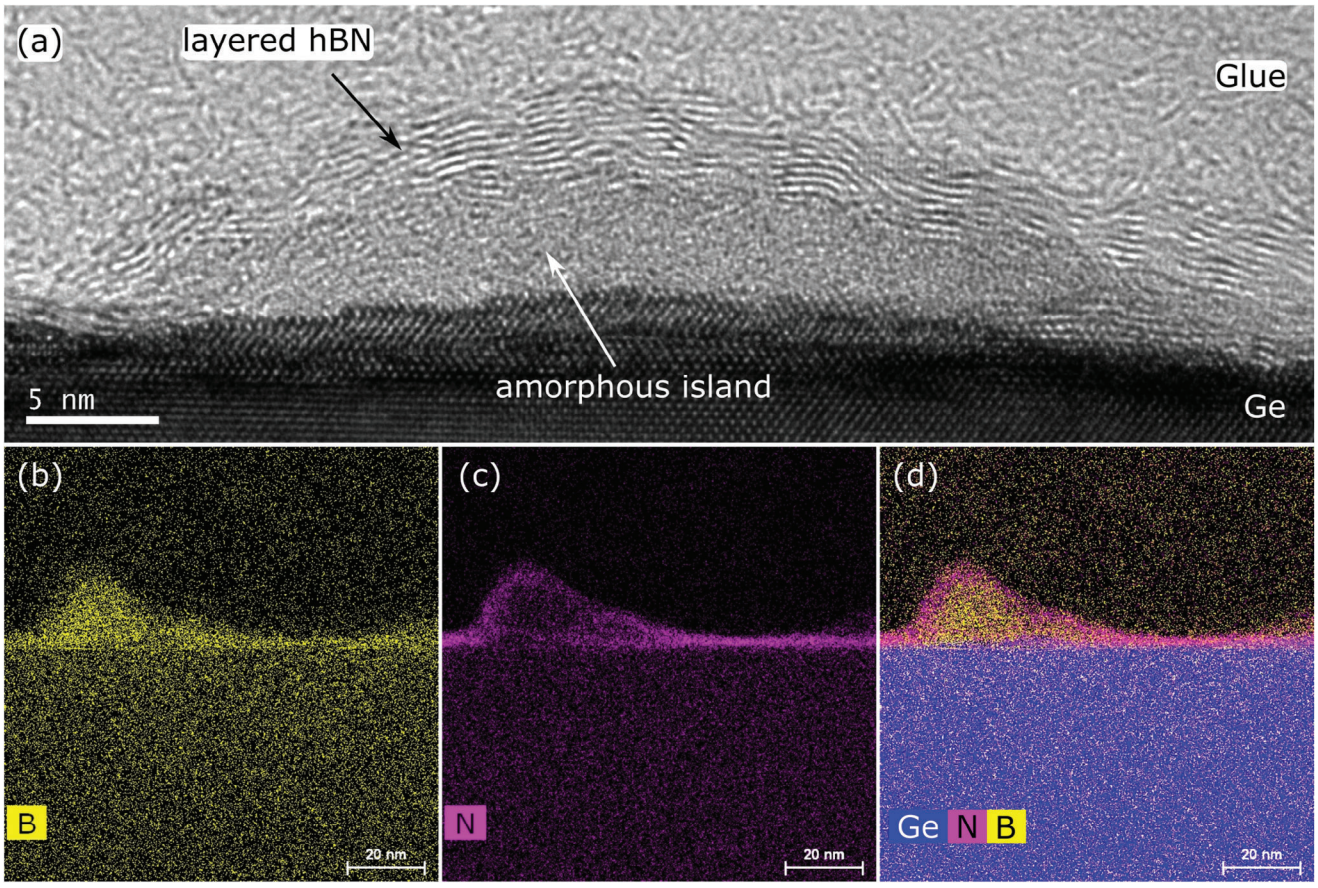

Figure 3. a) Cross section TEM image and b–d) EDX maps of small islands found in hBN films grown with Setup B.

time of only 10 min, after which the same amorphous, boron-rich islands were observed, but without the layered hBN overgrowth (see Figure S1, Supporting Information for more details). While this could point to some issues with the initial injection of the Ar/borazine mixture at the start of the growth phase, the exact origin of these islands is still unclear.

In an attempt to understand the mechanisms behind the suppression of the nanocrystalline islands, we take a look at pressure and temperature, as these are two of the most critical process parameters in CVD synthesis. While both parameters are identical globally for the studied reactor configurations, the resulting hBN films were shown to be markedly different. Therefore, temperature and pressure need to be examined on a more local scale. The change in geometry causes several possible effects: the additional space between the borazine inlet and the sample surface in the case of Setup B allows the gas to expand more and the pressure to equalize closer to the chamber background pressure before reaching the sample. This effect might result in a lower and more homogenous local pressure of the precursor at the sample surface, leading to slower and more homogeneous film growth. The increased distance of the inlet tube end to the heated sample and holder might also result in less passive heating of the tube and, subsequently, a lower precursor temperature before entering the reactor chamber. This may influence the pre-reactions of the borazine molecules, leading to different borazine-derived chemical species reaching the sample surface and participating in the growth process. Such gas phase reactions are not expected to be significant in the reactor itself due to the low chamber pressure,[38] but inside the thin injector tube, the pressure is much higher, as shown in **Figure** 4d,e. To evaluate whether the mentioned effects are sufficiently large to be significant for our setup, computational fluid dynamics simulations were conducted using COMSOL Multiphysics. A 2D model approximating the reactor geometry was constructed, including the borazine inlet tube, heated sample holder, and vacuum pump. A detailed description of the model can be found in the Supporting Information.

The simulations show that the difference in gas temperature before entering the reactor chamber is indeed significant. Figure 4a,b shows the computed spatial temperature distributions for Setup A and Setup B, respectively, in the immediate surroundings of the sample holder. If the borazine inlet is close to the hot sample surface, the end section is passively heated to several hundred degrees Celsius, mainly through radiation. For better illustration, Figure 4c plots the temperature along a straight line through the middle of the inlet tube up to the sample (last 20 cm only; see also blue line in the inset) for both setups. Generally, the gas heats up as it flows through the tube toward the reactor chamber, through heat transfer from the increasingly hot tube walls, up to 600 °C for Setup A and 430 °C for Setup B, see Figure 4c. As the gas enters the reactor chamber and flows toward the sample surface, it is directly heated by the hot sample

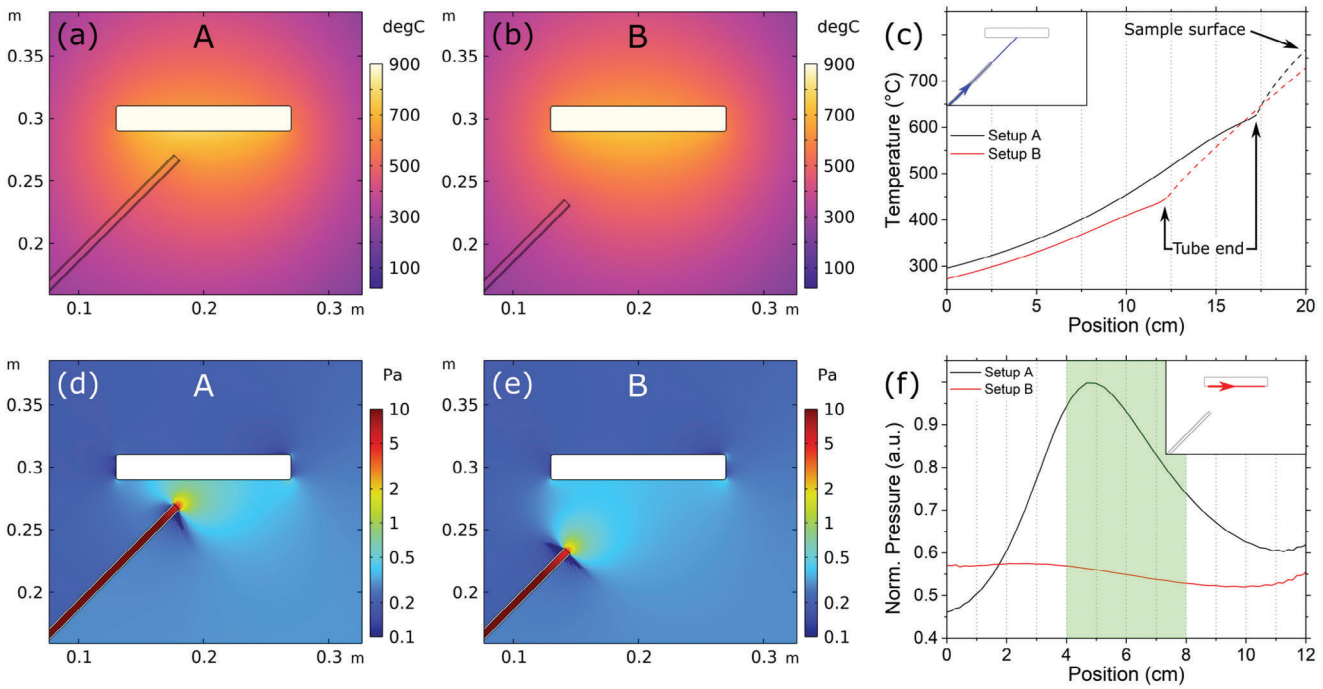

Figure 4. CFD simulation results. a,b) Spatial temperature distributions close to the sample holder for the two setups. c) Line plots of temperatures along the injector; the cutline is shown in the inset. d,e) Spatial pressure distributions close to the sample holder for the two setups. f) Line plots of normalized local pressure along the surface of the sample holder. The inset shows the cutline. The green color marks the area occupied by the actual sample.

holder, and the temperature increases more quickly (dashed line section in Figure 4c). The gas temperature does not equalize with the sample surface temperature of 900 °C at the end of the graph due to a heat flux perpendicular to the surface (the Smoluchowski temperature jump; see Supporting Information for more details). It should also be noted here that the 2D model is a simplified description of the experimental setup, so the absolute temperature values returned by the simulation are only an estimate and do not necessarily represent the precise conditions in the physical setup. Instead, the relative values between the two setups are more meaningful. With this in mind, a slightly higher overall gas temperature can be noted in the case of Setup A due to the increased heat flux to the injector tube. More importantly, the most significant difference is in the gas temperature at the respective outlets, which is almost 200 °C higher for Setup A (see positions marked in Figure 4c). This could facilitate gas phase reactions of the borazine precursor, which might result in the unwanted hBN nanocrystalline islands (see Figure 2a–c).

Early studies on the borazine compound found several polymerization and decomposition reactions at relatively low temperatures. For example, liquid borazine reacts to polyborazylene ($[B_3N_3H_4]_x$) via dehydropolymerization with high yields within 48 h at only 70 °C.[39] While the reaction rate would be several orders of magnitude lower due to the low borazine partial pressure in the injector (≈1 Pa, see Supporting Information), it cannot be entirely dismissed in the case of reactor setup A, because of the low-temperature requirement. Another study found that borazine vapor decomposes to nonvolatile $BNH_{0.8}$ and hydrogen gas at 340 – 381 °C.[40] Additionally, the formation of $B_5N_5H_8$ and $B_6N_6H_{10}$ dimers (naphthalene and diphenyl analogs, respectively), $B_3N_5H_8$ (2,4-diaminoborazine), as well as larger polymers, could be demonstrated from pyrolytic dehydrogenation of borazine vapor at 380 °C.[40] These species might lead to suboptimal hBN growth and facilitate the formation of nanocrystalline islands, which is mitigated by moving the borazine inlet to its position in Setup B.

Since the conditions in the injector differ from those in the abovementioned studies, especially in pressure, the plausibility of such polymerization was confirmed for our setup by ab initio calculations, which can be found in the Supporting Information. The equilibrium partial pressures of $B_5N_5H_8$ and $B_6N_6H_{10}$ were found to be significant (leading to a sample exposure of >1 L h^{-1}) at reasonable ranges of process conditions (temperatures, partial pressures of reaction partners). However, as the reaction pathways exhibit relatively high energy barriers (≈2 eV), the polymerization reactions are kinetically inhibited and would require catalysis. The hot walls of the injector are expected to provide a catalytic effect for these reactions, but this needs to be investigated in more detail in a future study.

The reactor configuration also affects the local pressure – and therefore molecule density – of the carrier gas/precursor mixture at the sample surface. The computed spatial pressure distributions for Setup A and Setup B, respectively, are shown in Figure 4d,e. The gas expansion zone is clearly visible, resulting in a region of elevated pressure compared to the surrounding chamber extending to the sample surface for both cases. Figure 4f plots the pressure along the surface of the sample holder (see also red line in the inset) for both setups, normalized to the maximum value for Setup A. In the case of the injector tube ending very

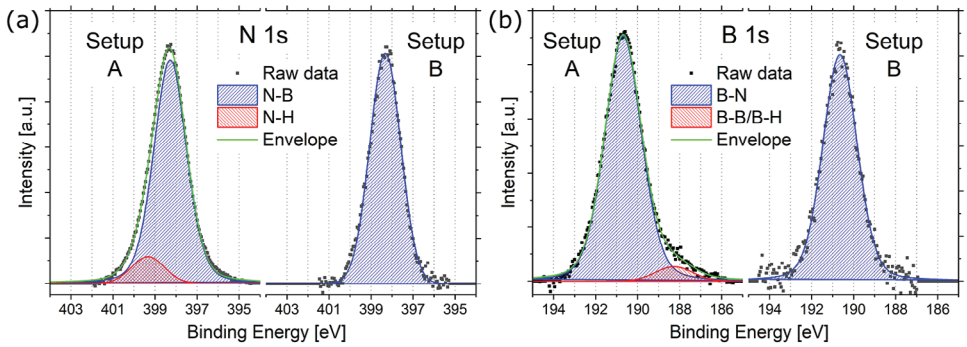

Figure 5. a) N 1s and b) B 1s XPS spectra of hBN films grown with both reactor setups.

close to the sample surface (Setup A), a strongly non-uniform pressure distribution is observed, with a maximum near the center of the sample holder. The pressure decreases steadily toward the edges to ≈50 % of the maximum value. On the other hand, Setup B results in a broader and flatter distribution with an overall reduced pressure in the range of ≈55% of the maximum value for Setup A. This difference is exacerbated when only the section of the sample holder actually occupied by the sample is considered (green area in Figure 4f). Here, the average normalized pressure is 0.899 for Setup A, and the overall range (the difference between the maximum and minimum pressure at the sample surface) is 0.284. For Setup B, the average normalized pressure is 0.547, with an overall range of 0.041, yielding a 39% reduction of average pressure and an 86% reduction of pressure variability. These results corroborate the initial hypothesis that Setup B leads to a lower and more homogeneous local pressure at the sample surface. Assuming operation in the diffusion/mass transport limited growth regime, this plausibly contributes to the observed changes in film thickness and structure. At high growth temperatures, growth rates are not kinetically limited by the surface reaction rate but rather by the transport of reactive species to the sample surface, which benefits from increased precursor partial pressure. This is especially true for very low reactor pressures (as in our setup), where diffusion coefficients become large and, consequently, diffusion through the boundary layer above the sample surface is fast.[38] Typically, the mass transport limited regime ranges from several hundred to about a thousand degrees Celsius,[41,42] so this is the expected behavior for our growth temperature of ≈900 °C, even though the exact surface reactions and corresponding reaction rates are unknown. Hence, the highest film thickness should occur at one edge of the sample, creating the symmetric thickness gradient depicted in Figure 1c due to the sample rotation during the growth process.

So far, it has been shown that the positioning of the borazine injector influences the local borazine partial pressure at the sample surface and its temperature while still in the injector. This leads to an observed change in growth mode from a mix of flat regions and islands of randomly oriented nanocrystallites to purely well-aligned, layered growth and reduces the overall growth rate. It should be noted that these effects are inherently intertwined and cannot be separated for individual experimental verification. The morphology and structure of the grown hBN films were characterized in detail on the microscopic scale.

Lastly, the stoichiometry and crystalline quality of the hBN films grown with both setups were also characterized on a more macroscopic scale, using XPS and Raman spectroscopy. The N 1s and B 1s XPS core level spectra are shown in **Figure 5**. Peak fitting was performed using a Tougaard background and Gaussian-Lorentzian line shapes. For the sample grown with Setup B, the spectra can be fitted with only one peak each, specifically at 398.3 and 190.6 eV, which can be attributed to N–B and B–N bonds, respectively.[43,44] The hBN film grown with Setup A exhibits additional peaks at 399.4 eV and 188.3 eV, corresponding to N–H and B–B/B–H bonds, respectively.[44,45] This indicates incomplete dehydrogenation reactions and possibly the formation of B–B point defects or B clusters in the case of Setup A, which could be a symptom of unfavorable borazine derivatives leading to suboptimal growth. Noticeably, no B–B bonds were detected in the case of Setup B despite the presence of the boron-rich, amorphous islands described above. This might be due to the thickness of the layered overgrowth exceeding the XPS information depth. In addition to a better hBN film structure and quality, Setup B also yields improved stoichiometry compared to Setup A, with N:B ratios of 1.07 and 1.26, respectively.

The crystalline quality was probed at 100 different positions in a 10 × 10 grid and a distance of 3 µm between each point. **Figure 6a** shows the average Raman spectrum for both setups. The characteristic hBN E_{2g} mode is observed at 1373.7 ± 0.8 cm^{-1} and 1372.2 ± 0.4 cm^{-1} for hBN films grown with Setup A and B, respectively. The peak positions are shifted upward with respect to bulk hBN (1366 cm^{-1}[46]), indicative of small crystallites or small amounts of compressive strain in the hBN film.[47,48] In the case of Setup B, small crystallites can be ruled out from the TEM investigation, but the difference in the thermal expansion coefficients of substrate and film can easily introduce strain. The FWHMs of the hBN peaks are 37.3 ± 2.9 cm^{-1} and 22.6 ± 1.2 cm^{-1} for Setup A and Setup B, respectively, further confirming the improved crystalline quality of the film grown by Setup B. Both the average FWHM and the variability (standard deviation) of the FWHM are reduced noticeably. Figure 6b plots the FWHM map for Setup B; a full comparison of the peak position and FWHM maps can be found in Figure S5 (Supporting Information). Note that in the case of Setup A, both nanocrystalline islands and layered hBN are present in the volume probed by the spectrometer (laser spot size ≈1 µm). Consequently, the nanoscale islands will likely dominate the hBN material under the Raman probe. Putting the results for Setup B into perspective,

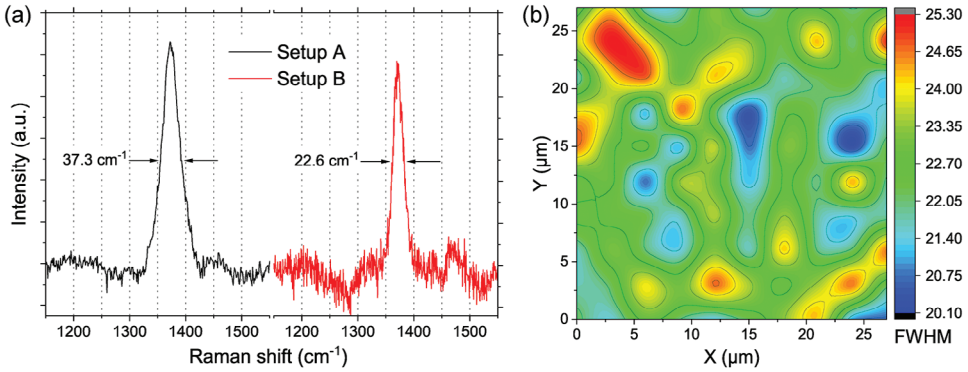

Figure 6. a) Raman spectra of hBN films grown with both reactor geometries. b) FWHM map for Setup B.

similar FWHM values in the range of 25–35 cm^{-1} have been reported for hBN films grown on other non-metal substrates, but these are primarily nanocrystalline films with thicknesses in the range of 0.3–2.3 μm,[17–19,49,50] while reports for nanometer thickness, layered hBN are scarcer.[22–25] These high-quality, metal-free hBN thin films will enable the fabrication of hBN/graphene/hBN heterostructures with superior graphene charge carrier mobility.

3. Conclusion

Two different reactor configurations were investigated for the chemical vapor deposition growth of hexagonal boron nitride on epitaxial Ge(001)/Si substrates. While the global chamber pressure and growth temperature were identical, changing the setup affected the hBN film structure and quality through changes in the local precursor partial pressure distribution near the sample surface and the precursor temperature before entering the reactor chamber. Setup A, which placed the borazine precursor injector tube very close to the sample surface, yielded hBN films containing both vertically stacked hBN layers and a large density of nanocrystalline islands, as observed by cross sectional TEM. The film thickness is inhomogeneous at the millimeter scale, which is attributed to an inhomogeneous pressure distribution at the sample surface found with the help of numerical CFD simulations. These simulations also show strong radiative heating of the injector tube near the hot sample holder, plausibly contributing to the formation of unwanted nanocrystalline islands via the creation of unfavorable borazine derivatives in gas phase reactions. For Setup B, on the other hand, the injector tube was moved away from the sample surface, resulting in well-aligned, layered growth of hBN without nanocrystalline islands. A much more homogeneous film thickness and overall reduced growth rate were observed, which is mirrored in the corresponding CFD simulations, showing a 39% reduction in average pressure and an 86% reduction in pressure variability on the sample surface. Additionally, the CFD simulations show that the maximum gas temperature in the injector is almost 200 °C lower compared to Setup A, drastically reducing gas phase reaction rates. The hBN films grown with Setup B exhibit Raman peaks with an FWHM of 23 cm^{-1}, on par with films grown on other non-metal substrates, but achieved at lower growth temperature and with a low thickness of only a few nm.

4. Experimental Section

Synthesis of hBN thin films on intrinsic, 2 μm thick epitaxial Ge(001)/Si substrates[37] was carried out in a RIBER Compact 21T ultra-high vacuum (UHV) CVD system at a setpoint temperature of 980 °C (corresponding to a surface temperature of ≈900 °C) and a pressure of 0.1 Pa using borazine ($B_3N_3H_6$, Katchem) as the precursor and Ar (99.9999 %, Air Liquide) as the carrier gas. For this study, the injector tube (5 mm diameter) supplying the precursor/carrier gas mixture to the reactor was placed in two different positions, with different distances to the sample surface: 3 and 8 cm. Samples were annealed in UHV (≈10^{-6} Pa) for 30 min at 900 °C to remove the native oxide. For hBN growth, 40 sccm of Ar flowed through the borazine bubbler, which was held at −10 °C. The growth time was 120 min unless specified otherwise, and afterward, the samples were rapidly cooled down to room temperature.

In situ X-ray photoelectron spectroscopy (SPECS GmbH) with an Al Kα X-ray source was used to investigate the chemical composition. The quality of the hBN thin films was characterized using Raman spectroscopy (Renishaw inVia, 532 nm excitation wavelength, spot diameter ≈1 μm). Raman spectra were referenced to the Si peak at 520.5 cm^{-1}. The crystalline structure was studied by transmission electron microscopy (FEI Tecnai Osiris, 200 kV acceleration voltage). Energy-dispersive X-ray spectroscopy and electron energy loss spectroscopy were used in the scanning TEM mode to study the spatial distribution of boron and nitrogen. Atomic force microscopy (Bruker Dimension Icon) was performed to characterize the morphology of the samples.

To gain insight into the effect of the reactor setup on the precursor gas flow, computational fluid dynamics simulations were performed in two dimensions using the Slip Flow interface in COMSOL Multiphysics. The interface uses the Navier–Stokes equations to model the gas flow, with modified boundary conditions to account for the wall-adjacent Knudsen layer. It also contains the heat flow equations to model conductive and convective thermal effects. The Surface-to-Surface Radiation interface was coupled with the Slip Flow interface to include radiation. More details can be found in the Supporting Information.

The plausibility of certain chemical reactions was verified by ab initio calculations using the method described in Ref. [34].

Supporting Information

Supporting Information is available from the Wiley Online Library or from the author.

Acknowledgements

This work was funded by the FLAG-ERA 2019 grant 2DHetero by the Deutsche Forschungsgemeinschaft (DFG, German Research Foundation)

– 436545422. The authors also gratefully acknowledge the support of the Fonds de la Recherche Scientifique de Belgique (F.R.S.-FNRS) and the EU for funding the 2DHetero FLAG_ERA project (Grant No. 8009.19) and the Gauss Centre for Supercomputing e.V. (www.gauss-centre.eu) for funding this project by providing computing time through the John von Neumann Institute for Computing (NIC) on the GCS Supercomputer JUWELS at Jülich Supercomputing Centre (JSC).

Conflict of Interest

The authors declare no conflict of interest.

Data Availability Statement

The data that support the findings of this study are available from the corresponding author upon reasonable request.

Keywords

2D materials, CFD simulations, chemical vapor deposition, CVD, hexagonal boron nitride

Received: May 27, 2024
Revised: September 20, 2024
Published online:

[1] K. Watanabe, T. Taniguchi, T. Niiyama, K. Miya, M. Taniguchi, *Nat. Photon* **2009**, *3*, 591.
[2] R. Dahal, J. Li, S. Majety, B. N. Pantha, X. K. Cao, J. Y. Lin, H. X. Jiang, *Appl. Phys. Lett.* **2011**, *98*, 211110.
[3] L. Britnell, R. V. Gorbachev, R. Jalil, B. D. Belle, F. Schedin, M. I. Katsnelson, L. Eaves, S. V. Morozov, A. S. Mayorov, N. M. R. Peres, A. H. C. Neto, J. Leist, A. K. Geim, L. A. Ponomarenko, K. S. Novoselov, *Nano Lett.* **2012**, *12*, 1707.
[4] L. Britnell, R. V. Gorbachev, A. K. Geim, L. A. Ponomarenko, A. Mishchenko, M. T. Greenaway, T. M. Fromhold, K. S. Novoselov, L. Eaves, *Nat. Commun.* **2013**, *4*, 1794.
[5] C. R. Dean, A. F. Young, I. Meric, C. Lee, L. Wang, S. Sorgenfrei, K. Watanabe, T. Taniguchi, P. Kim, K. L. Shepard, J. Hone, *Nat. Nanotechnol.* **2010**, *5*, 722.
[6] A. S. Mayorov, R. V. Gorbachev, S. V. Morozov, L. Britnell, R. Jalil, L. A. Ponomarenko, P. Blake, K. S. Novoselov, K. Watanabe, T. Taniguchi, A. K. Geim, *Nano Lett.* **2011**, *11*, 2396.
[7] L. Wang, I. Meric, P. Y. Huang, Q. Gao, Y. Gao, H. Tran, T. Taniguchi, K. Watanabe, L. M. Campos, D. A. Muller, J. Guo, P. Kim, J. Hone, K. L. Shepard, C. R. Dean, *Science* **2013**, *342*, 614.
[8] M. Schmitz, S. Engels, L. Banszerus, K. Watanabe, T. Taniguchi, C. Stampfer, B. Beschoten, *Appl. Phys. Lett.* **2017**, *110*, 263110.
[9] S. M. Kim, A. Hsu, M. H. Park, S. H. Chae, S. J. Yun, J. S. Lee, D.-H. Cho, W. Fang, C. Lee, T. Palacios, M. Dresselhaus, K. K. Kim, Y. H. Lee, J. Kong, *Nat. Commun.* **2015**, 6.
[10] R.-J. Chang, X. Wang, S. Wang, Y. Sheng, B. Porter, H. Bhaskaran, J. H. Warner, *Chem. Mater.* **2017**, *29*, 6252.
[11] H. Jeong, D. Y. Kim, J. Kim, S. Moon, N. Han, S. H. Lee, O. F. N. Okello, K. Song, S.-Y. Choi, J. K. Kim, *Sci. Rep.* **2019**, *9*, 5736.
[12] T.-A. Chen, C.-P. Chuu, C.-C. Tseng, C.-K. Wen, H.-S. P. Wong, S. Pan, R. Li, T.-A. Chao, W.-C. Chueh, Y. Zhang, Q. Fu, B. I. Yakobson, W.-H. Chang, L.-J. Li, *Nature* **2020**, *579*, 219.
[13] S. Fukamachi, P. Solís-Fernández, K. Kawahara, D. Tanaka, T. Otake, Y.-C. Lin, K. Suenaga, H. Ago, *Nat. Electron.* **2023**, *6*, 126.
[14] M. S. Bresnehan, M. J. Hollander, M. Wetherington, M. LaBella, K. A. Trumbull, R. Cavalero, D. W. Snyder, J. A. Robinson, *ACS Nano* **2012**, *6*, 5234.
[15] A. Ambrosi, M. Pumera, *Nanoscale* **2014**, *6*, 472.
[16] G. Lupina, J. Kitzmann, I. Costina, M. Lukosius, C. Wenger, A. Wolff, S. Vaziri, M. Östling, I. Pasternak, A. Krajewska, W. Strupinski, S. Kataria, A. Gahoi, M. C. Lemme, G. Ruhl, G. Zoth, O. Luxenhofer, W. Mehr, *ACS Nano* **2015**, *9*, 4776.
[17] X. Chen, H. Sun, W. Zhang, C. Tan, X. Liu, J. Zhao, L. Hou, Y. Gao, J. Song, Z. Chen, *Vacuum* **2022**, *199*, 110935.
[18] R. Singhal, E. Echeverria, D. N. McIlroy, R. N. Singh, *Thin Solid Films* **2021**, *733*, 138812.
[19] X. Chen, C. Tan, X. Liu, K. Luan, Y. Guan, X. Liu, J. Zhao, L. Hou, Y. Gao, Z. Chen, *J. Mater. Sci.: Mater. Electron.* **2021**, *32*, 3713.
[20] A.-R. Jang, S. Hong, C. Hyun, S. I. Yoon, G. Kim, H. Y. Jeong, T. J. Shin, S. O. Park, K. Wong, S. K. Kwak, N. Park, K. Yu, E. Choi, A. Mishchenko, F. Withers, K. S. Novoselov, H. Lim, H. S. Shin, *Nano Lett.* **2016**, *16*, 3360.
[21] X. Li, S. Sundaram, Y. El Gmili, T. Ayari, R. Puybaret, G. Patriarche, P. L. Voss, J. P. Salvestrini, A. Ougazzaden, *Cryst. Growth Des.* **2016**, *16*, 3409.
[22] S. Saha, A. Rice, A. Ghosh, S. M. N. Hasan, W. You, T. Ma, A. Hunter, L. J. Bissell, R. Bedford, M. Crawford, S. Arafin, *AIP Adv.* **2021**, *11*, 55008.
[23] D. Chugh, J. Wong-Leung, L. Li, M. Lysevych, H. H. Tan, C. Jagadish, *2D Mater.* **2018**, *5*, 045018.
[24] A. K. Dąbrowska, M. Tokarczyk, G. Kowalski, J. Binder, R. Bożek, J. Borysiuk, R. Stępniewski, A. Wysmołek, *2D Mater.* **2021**, *8*, 015017.
[25] M. Tokarczyk, A. K. Dąbrowska, G. Kowalski, R. Bożek, J. Iwański, J. Binder, R. Stępniewski, A. Wysmołek, *2D Mater.* **2023**, *10*, 025010.
[26] L. H. Li, E. J. G. Santos, T. Xing, E. Cappelluti, R. Roldán, Y. Chen, K. Watanabe, T. Taniguchi, *Nano Lett.* **2015**, *15*, 218.
[27] P. W. Loscutoff, S. F. Bent, *Annu. Rev. Phys. Chem.* **2006**, *57*, 467.
[28] G. Wang, M. Zhang, Y. Zhu, G. Ding, Da Jiang, Q. Guo, S. Liu, X. Xie, P. K. Chu, Z. Di, X. Wang, *Sci. Rep.* **2013**, *3*, 2465.
[29] M. Lukosius, J. Dabrowski, J. Kitzmann, O. Fursenko, F. Akhtar, M. Lisker, G. Lippert, S. Schulze, Y. Yamamoto, M. A. Schubert, H. M. Krause, A. Wolff, A. Mai, T. Schroeder, G. Lupina, *ACS Appl. Mater. Interfaces* **2016**, *8*, 33786.
[30] J. Aprojanz, P. Rosenzweig, T. T. N. Nguyen, H. Karakachian, K. Küster, U. Starke, M. Lukosius, G. Lippert, A. Sinterhauf, M. Wenderoth, A. A. Zakharov, C. Tegenkamp, *ACS Appl. Mater. Interfaces* **2020**, *12*, 43065.
[31] J. Yin, X. Liu, W. Lu, J. Li, Y. Cao, Y. Li, Y. Xu, X. Li, J. Zhou, C. Jin, W. Guo, *Small* **2015**, *11*, 5375.
[32] M.-K. Hong, S.-H. Hyun, H.-S. Jang, B.-S. An, H.-C. Jang, H.-S. Hwang, S.-I. Kim, J.-Y. Moon, S. M. Sattari-Esfahlan, S.-Y. Lee, S.-K. Son, D. Whang, J.-H. Lee, *Appl. Surf. Sci.* **2021**, 554.
[33] C. Zhang, B. Gao, Y. Ran, Z. Shi, H. Zhu, H. Zhang, J. Liu, B. Yang, Z. Liu, T. Wu, X. Xie, *2D Mater.* **2021**, *8*, 035041.
[34] M. Franck, J. Dabrowski, M. A. Schubert, C. Wenger, M. Lukosius, *Nanomaterials* **2022**, *12*, 3260.
[35] M. D. Allendorf, T. M. Besmann, R. J. Kee, M. T. Swihart, *Chemical Vapour Deposition: Precursors, Processes and Applications* (Eds: A. C. Jones, M. L. Hitchman), RSC Publishing, Cambridge **2009**, p-93.
[36] S.-Y. Lee, T.-Y. Jeong, S. Jung, K.-J. Yee, *Phys. Status Solidi B* **2019**, *256*, 1800417.
[37] Y. Yamamoto, P. Zaumseil, T. Arguirov, M. Kittler, B. Tillack, *Solid-State Electron.* **2011**, *60*, 2.
[38] A. C. Jones, M. L. Hitchman, *Chemical Vapour Deposition: Precursors, Processes and Applications* (Eds: A. C. Jones, M. L. Hitchman), RSC Publishing, Cambridge **2009**, p-1.
[39] P. J. Fazen, J. S. Beck, A. T. Lynch, E. E. Remsen, L. G. Sneddon, *Chem. Mater.* **1990**, *2*, 96.

[40] A. W. Laubengayer, P. C. Moews, R. F. Porter, *J. Am. Chem. Soc.* **1961**, *83*, 1337.
[41] S. D. Hersee, J. P. Duchemin, *Annu. Rev. Mater. Sci.* **1982**, *12*, 65.
[42] J. J. Coleman, *Proc. IEEE* **1997**, *85*, 1715.
[43] R. Trehan, Y. Lifshitz, J. W. Rabalais, *J. Vac. Sci. Technol., A* **1990**, *8*, 4026.
[44] *Handbook of X-ray Photoelectron Spectroscopy: A Reference Book of Standard Spectra for Identification and Interpretation of XPS Data*, (Ed: J. Chastain), Physical Electronics Division, Perkin-Elmer Corporation, Eden Prairie, MN. **1995**.
[45] T. Goto, T. Hirai, *J. Mater. Sci. Lett.* **1988**, *7*, 548.
[46] T. Kuzuba, K. Era, T. Ishii, T. Sato, *Solid State Commun.* **1978**, *25*, 863.
[47] Q. Cai, D. Scullion, A. Falin, K. Watanabe, T. Taniguchi, Y. Chen, E. J. G. Santos, L. H. Li, *Nanoscale* **2017**, *9*, 3059.
[48] R. J. Nemanich, S. A. Solin, R. M. Martin, *Phys. Rev. B* **1981**, *23*, 6348.
[49] K. Ahmed, R. Dahal, A. Weltz, J.-Q. Lu, Y. Danon, I. B. Bhat, *Appl. Phys. Lett.* **2016**, *109*, 113501.
[50] K. Ahmed, R. Dahal, A. Weltz, J. J.-Q. Lu, Y. Danon, I. B. Bhat, *Mater. Res. Express* **2017**, *4*, 015007.